

PAPER

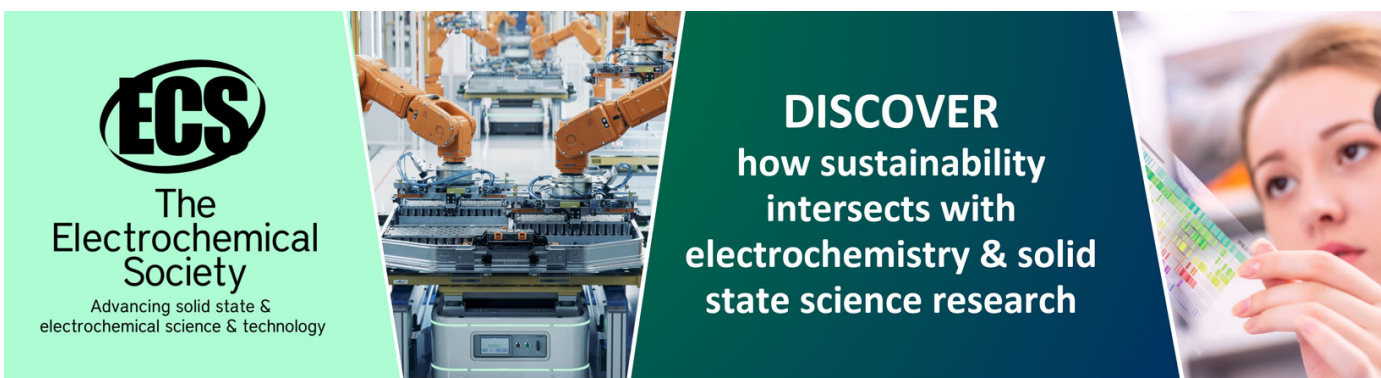
Multimode coaxial extrusion of segmented core-shell structures for soft metamechanics and biomimetic applications

To cite this article: Jiawen Xu *et al* 2024 *Smart Mater. Struct.* **33** 015003

View the [article online](#) for updates and enhancements.

You may also like

- [Triboelectric 'electrostatic tweezers' for manipulating droplets on lubricated slippery surfaces prepared by femtosecond laser processing](#)
Jiale Yong, Xinlei Li, Youdi Hu *et al.*
- [The bioengineering of perfusable endocrine tissue with anastomosing blood vessels](#)
Hiroki Yago, Jun Homma, Hidekazu Sekine *et al.*
- [Micro-sized droplet formation by interaction between dielectric barrier discharge and liquid](#)
Ryosuke Watanabe, Natsuki Sugata and Daisuke Yoshino



ECS
The
Electrochemical
Society
Advancing solid state &
electrochemical science & technology

DISCOVER
how sustainability
intersects with
electrochemistry & solid
state science research

Multimode coaxial extrusion of segmented core-shell structures for soft metamechanics and biomimetic applications

Jiawen Xu¹ , Yanbing Cao¹, Zhenyu Wang¹ , Heng-Yong Nie^{2,3} , Xiaolong Wang^{4,*}  and Yu Liu^{1,*} 

¹ School of Mechanical Engineering, Jiangnan University, Wuxi 214122, People's Republic of China

² Surface Science Western, The University of Western Ontario, London, ON N6G 0J3, Canada

³ Department of Physics and Astronomy, The University of Western Ontario, London, ON N6A 3K7, Canada

⁴ Lanzhou Institute of Chemical Physics, Chinese Academy of Sciences, Lanzhou 730000, People's Republic of China

E-mail: wangxl@licp.cas.cn and yuliu@jiangnan.edu.cn

Received 14 May 2023, revised 24 October 2023

Accepted for publication 23 November 2023

Published 1 December 2023



CrossMark

Abstract

The unique ability to combine versatile materials via additive manufacturing greatly enhances the functionalities of soft machines. However, manufacturing for multi-material devices often involves complex and redundant procedures. Herein, we develop a multimode coaxial direct ink writing method for efficient 3D printing of multi-material filaments in the form of core-shell material distribution at millimeter scales. Through simulations and experiments, essential printing parameters, such as extrusion pressure and deposition speed combinations, are investigated to control compositions simultaneously. As exemplars, we fabricate soft lattices presenting tunable mechanical responses by printing soft and tough silicone in a single pass. We also demonstrate bio-mimetic potentials by fabricating soft fingers and magnetic shape-shifting structures with multiple functional materials. Our method is expected to provide a new paradigm for designing and manufacturing the rapid prototyping of soft functional machines.

Supplementary material for this article is available [online](#)

Keywords: coaxial 3D printing, functional soft materials, bioinspired soft machine

1. Introduction

Soft materials, with natural flexibility and biocompatible properties, are increasingly relevant to emerging technologies in medical devices [1–3], wearable textiles [4–7], soft robotics [8–11] and bionic technology [12–14]. Moreover, there have

been a great number of studies in soft functional materials have demonstrated their applicability on sensing [15–17], luminescence [18], and shape-shifting [19, 20], showing extraordinary advantage and performance [21, 22]. Although plenty of manufacturing methods such as cutting, casting [23, 24], bonding [25], folding [26], knitting and weaving [27–29] or combinations [12, 30, 31] allow to obtain soft device with exquisite details, manufacturing procedures still are time-consuming, complex and redundant for shapes or materials diversity.

* Authors to whom any correspondence should be addressed.

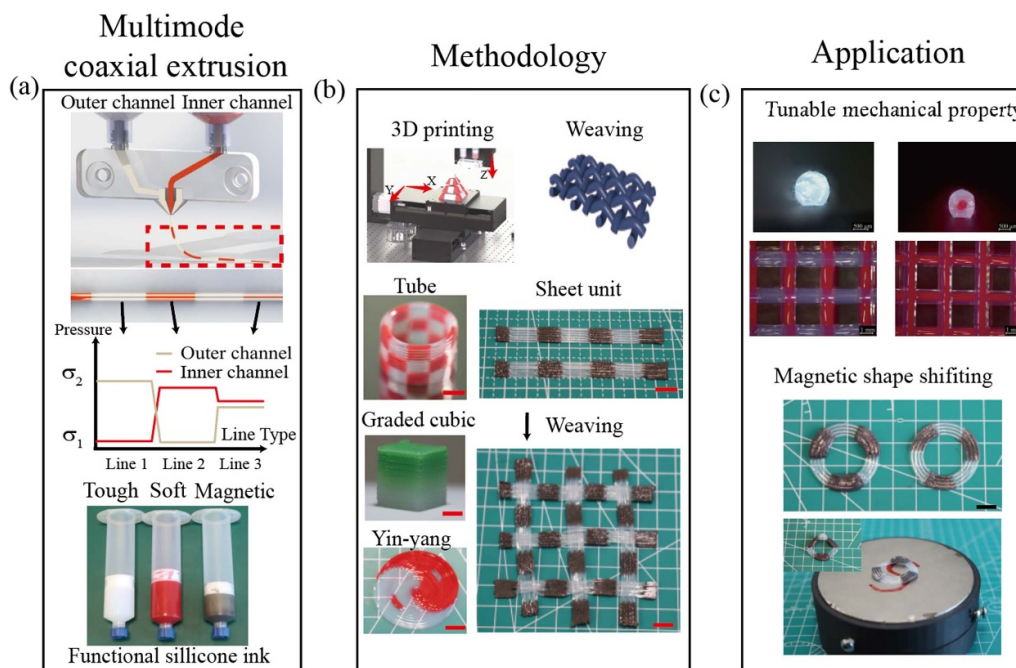


Figure 1. Illustration of the mcDIW including the extrusion process, methodology based on that and applications. (a) Schematic diagram of multimode coaxial extrusion actuated by pneumatic waveform using functional multiple inks. (b) Direct 3D printing or weaving based on multimode extrusion and multi-material sample exhibition such as tube, graded cubic, yin–yang pattern or magnetic sheet unit, scale bars: 10 mm. (c) Applications of multi-material objects, such as tunable stiffness lattice and magnet-driven architecture.

Recently, 3D printing has attracted tremendous attention in patterning a broad palette of high-performance materials [32, 33], which can build the interior structures [34, 35] in the assembly-free approach [36–39]. Direct ink writing (DIW), an extrusion-based 3D printing technique, is facile and compatible for soft devices addressing gel-like materials [40–42]. Nevertheless, challenges, such as low efficiency during switching nozzles or ink [40, 43] or long material transitions of online mixing [44–46], are still remaining. Multi-material DIW based on fluidic strategy is executable. But due to complex extrusion control [5, 47–50], it presents limitations on producing functional filaments or products with complicated shapes.

Herein, as illustrated in figure 1, we have innovatively developed a novel multimode coaxial DIW (mcDIW) method with a multi-channel printhead (see figure S1), of which outlets is in concentric form. Such printhead is capable of depositing two functional materials, each of which flows through the individual channel, which is connected to the ink reservoir that can be individually actuated by digitally controlled pneumatic pressures. The core-shell or segmented filaments, whose compositions are determined by specific pressure combinations, can be produced in one pass deposition. Furthermore, we have demonstrated that the mcDIW is able to print multimaterials objects or unit for other technology e.g. weaving. To demonstrate the scalability of the method, soft, tough and magnetic silicone inks are utilized to construct lattices having tunable stiffness or bioinspired architecture such as soft finger or magnetic driven shape shifting sheets, respectively.

2. Experimental section

2.1. Printing system and processes

The printhead was built using an SLA printer (form 3, Formlabs, USA) load with High Temp V2 resin, the detailed design drawing is presented in figure S1. This printhead features a standard Luer lock for connection with syringe and mounting holes to install upon motion stage. Pneumatic pressure was adjusted by an electronic pressure valve (SMC ITV2050, Japan). All printing trajectories and procedures were generated using self-defined Gcode executed with LabVIEW and C#. Samples were printed on glass substrates, followed by a thorough cleaning with ethanol and subsequent drying. Then 3D printed samples were cured in an oven at 90 °C for 2 h.

2.2. Materials

In the validation experiments, the ink was SE1700 (Dow Corning, USA), prepared by mixing the base agent and catalyst agent in a weight ratio of 10:1 using a planetary mixer (ZYMC-180 V, ZYE Technology Co., Ltd) operated at 2000 r.p.m. for 3 min. To distinguish the ink from the different channel, core ink was dyed with a red pigment. As for the application experiments, the softer ink was a silicone formulated by homogeneously blending fumed SiO₂ (Aladdin Biochemical Technology Co., Ltd, Shanghai), Ecoflex 30 Part A and Part B (Smooth on, USA), and a red pigment at a

weight ratio of 0.18:1:1:0.1 using a planetary mixer operated at 2000 r.p.m. for 3 min. The tougher silicone used was abovementioned SE1700. The magnetic ink was formulated by mixing the following components at a weight ratio of 10:1:4:25: (1) SE 1700, (2) SE1700 cure agent, (3) Ecoflex 30 Part B, (4) NdFeB microparticles having an average diameter of 25 μm (Ax-Y4, Qinghai Tairui Mining Co., Ltd). The blender then was magnetized by impulse magnetic fields (5.7 T) generated by a magnetizer (MA-3030, Shenzhen JIUJUK Industrial Equipment Co. Ltd) to impart polarities on ferromagnetic particles. All printable inks were centrifuged at 5000 r.p.m. for 5 min to defoam in syringe before printing.

2.3. Characterizations

The rheological properties including viscosity and modulus of the inks were assessed via a rheometer (DHR-2, TA instrument). The testing fixture adopted was a cone plate with a cone angle of 2° and a 40 mm in diameter. The gap distance between the cone and substrate was set as 200 μm . The viscosity-shear rate relationship was determined by the ‘Flow Sweep’, where the range of shear rate was set as $0.1\text{--}1000\text{ s}^{-1}$. The modulus-shear stress relationship was obtained by applying stress from 0 to 1000 Pa, with the oscillation frequency set at 1 Hz. The characterization and measurement of geometry dimensions of printed samples were conducted on an optical microscope (DVM6 A, Leica Microsystems GmbH). A universal testing machine (QingJi QJ211, Shanghai) was used for mechanical testing. A handheld gauss meter (KT-101, Shenzhen Aokete Technology Co., Ltd) equipped with a Hall sensor detector was used to quantify magnetic field strength. Permanent magnetic prisms with dimensions of 40 mm \times 10 mm \times 5 mm were utilized to generate magnetic fields for orientation of the NdFeB and driving inchworm-like robots and shape-shifting sheets.

2.4. Finite element simulation method

To explore coaxial flow behavior, a computational model was developed using COMSOL Multiphysics 5.5. Here, the two-phase flow, phase field coupling feature set was used, which enables volume and velocity tracking of two flows. Meanwhile, Herschel–Bulkley model was utilized to capture the non-Newtonian viscoelastic flow properties, of which parameters such as density, fluid consistency coefficient (\mathbf{m}), flow behavior index (\mathbf{n}), yield stress (τ_0) were listed in table S1. Mechanical simulation of filaments (see figure 6(a)) and soft robots (see figure 6(b)) were conducted using COMSOL as well, while simulation of the soft lattice (figures 5(b) and (c)) was experimented with Abaqus because of its explicit algorithms for improved convergence. The constitute model of silicone was fitted using the Mooney–Rivlin constitutive whose two parameters (C_{10} and C_{01}) were fitted by uniaxial test data of printed Ecoflex 30/SiO₂ and SE1700 standard specimens (see figure S5 and table S2). The dimensions of simulations in software closely matched those of the actual objects.

3. Results and discussions

3.1. Switchable extrusion mode and deposition

At first, simulations are conducted to gain a deeper understanding of coaxial extrusion. To enhance the efficiency of the investigation, as depicted in figures 2(a) and (b), the rotational symmetry model around outlet is set up. As shown in figure 2(a), P_{in} and P_{out} denote applied pressure on core and shell inks, respectively. The desired indices, such as velocity and volume proportion, are exacted from the result in 2nd outlet plane. As a result, generally, core/shell width ratio rises as the P_{in} increased at each fixed P_{out} , as well as P_{out} decreased at each fixed P_{in} . Shell width is mainly decided by dimension of 2nd outlet, while core width is related to pressure combinations. Interestingly, this ratio exhibits an initial increase followed by a decrease, as P_{out} sore from 0 to 30 kPa when keep unchanged P_{in} at low values, e.g. 8 or 10 kPa. We infer that the phenomenon occurred because the core ink would be pushed from inner channel then slowed down and accumulated in the zone between 1st and 2nd outlet. Then, as P_{out} increased during initial stage, shell ink with slow flow rate would aid in moving core ink, but reversely blocked core ink as flow rate of shell ink reached a high level. From figure 2(d) that presents the flow rate result with different pressure combinations, it is evident that both P_{out} and P_{in} are positively correlated with flow rate, with P_{out} having a more significant effect. In addition, figure 2(e) provides insight into ink volume fraction and velocity distribution at the specific pressure combination (marked in figures 2(c) and (d)), offering more detailed results regarding the interaction of multiple materials. The simulation data suggests that controlling multi-materials extrusion through pneumatic manipulation is feasible. However, due to the lack of whole extrusion system’s simulation, it should be noted that the pressure used in simulation only serve as references for further experiments.

For further verification, SE1700 and dyed SE1700 were coaxially printed in the concurrent mode, in which both the inner and outer channels are simultaneously pressurized. In the section, the filament is collected by fixing the printhead at a high enough level to avoid pressing filament between the printhead and substrate. As depicted in figures 3(a)–(c), segmented filaments were printed in the alternating mode, alternatingly pressurized according to the pressure waveform (see figure 3(a)) with the same period ($T_1 = T_2$) (see video S1). As a result, there were red and translucent filaments whose length of each segment could be regulated by changing the period T_1 or T_2 , respectively. As shown in figure 2(c), the segment length determined by pressure duration T from 50 to 500 ms ranged from 1 to 8 mm. However, it must be pointed out that when T is less than 300 ms (corresponding to a segment of ~ 3 mm), the neighboring red segment was not well separated. We deduce that the original ink occupies the zone between two outlets of the channel, which would result in such a phenomenon that the segment volume became lower than the zone volume.

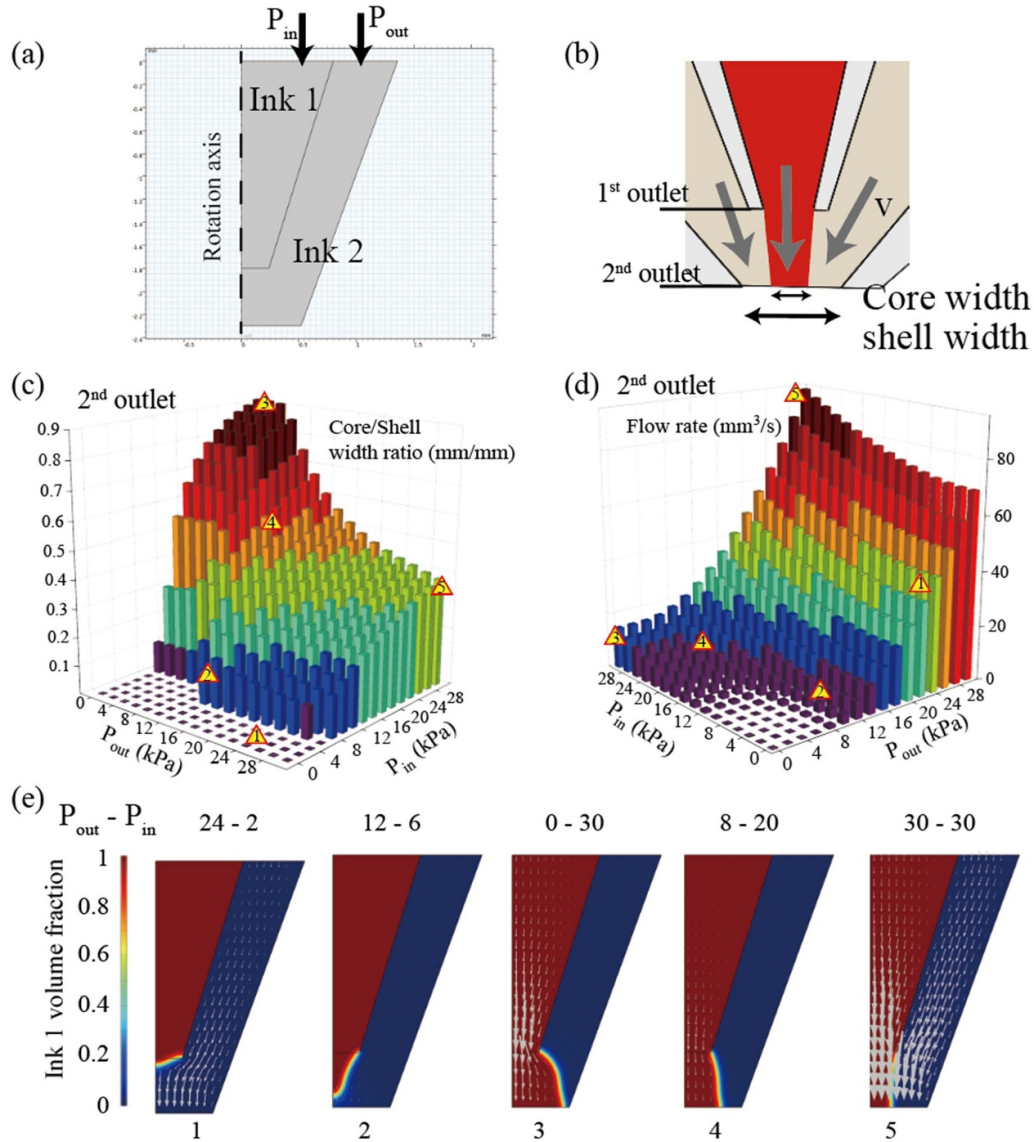


Figure 2. The simulation for multimode coaxial extrusion. (a) The rotational symmetry model for simplification, with dimensions matching the experimental printhead. (b) The illustration graph of the outlets for core/shell width and indices. (c) The relationship between core/shell width ratio and pressure combinations. (d) The relationship between the flow rate and different pressure combinations. (e) Diagram of fluid volume and flow rate distribution at the specific pressure combination, indicated by a triangle in (c) and (d).

Thixotropy of ink (shown in figure S4) suggested that the ink could not bear impacts caused by high-frequency pressure switching, which led to unstable rheological states. This delay reaction further caused mismatches in the deposition of materials from the designed position, which could be compensated by alerting pressure in advance.

As shown in figures 3(e)–(g), the concurrent mode printing forms coaxial filaments, where the red ink from the inner channel is embedded in the translucent ink from the outer channel. Figure 3(e) shows that increasing the pressure of the inner channel (P_{in}) from 0 to 300 kPa when fixed P_{out} at 200 kPa, induces that in core (red) with diameters d ranging from 0 to $\sim 1000 \mu\text{m}$ and shell with a fluctuating diameter D around $1100 \mu\text{m}$, respectively. The photographs in figure 3(f) show the side view (top row) and cross-sections (bottom row) of three coaxial filaments (top row) under P_{ch-in} of 0, 100,

and 310 kPa, respectively, when at fixed P_{out} of 200 kPa. It is confirmed that the pressure combinations determine the core/shell width ratio, while D is determined by the size of the printhead outlet, which coincides with the simulation result.

The deposition process is more complicated compared to extrusion since the collapse of inks between the printhead and substrate have to be considered. In the main, the dimensions of the printed filament are influenced by several factors, including standoff distance, printing speed and pneumatic pressure. Therefore, considering the mass equation, the line width of the printed filament is related to the formulation [51], $D = \sqrt{\frac{\Omega}{v}}$, where D denotes the shell width, v is the deposition speed, Ω corresponds to the flow rate which is severely determined by the applied pressure. As shown in figure 3(g), we carried out experiments that changing the speed from 6 to 9 mm s^{-1} and applied outer channel pressure from 80 to 110 kPa at

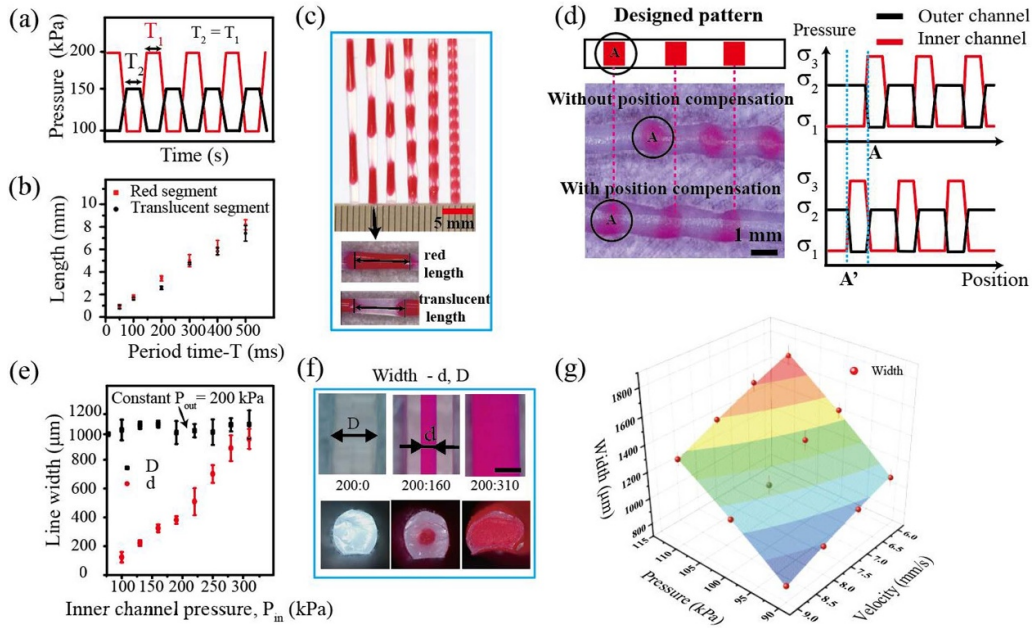


Figure 3. The concurrent and alternating printing modes for fabricating coaxial and segmented filaments. (a) Pressure waveforms illustration of alternating mode (black for P_{out} and red for P_{in}); (b) the relationship between segment time and length; (c) photographs of multi-material segmented filament and length measurement; (d) deposition at the designed position via pressure waveform adjustment; (e) the relationship between pressure and line width. (f) Photographs of coaxial filaments with side and cross section view, scale bar: 500 μm . (g) The shell width as a function of P_{out} pressure and deposition velocity without P_{in} .

fixed standoff distance of 1.1 mm resulting in filaments with their widths ranging 0.8–1.8 mm. Specifically, the printhead with a high deposition speed dragged the viscoelastic ink to thin the filament. Nevertheless, discontinuity in printed filament occurred when pressures set lower than 80 kPa, leading to insufficient ink even at the speed of 6 mm s^{-1} . Conversely, high flow rate caused by bigger pressures and low deposition speed would cause accumulation of ink to enlarge filament width. Summarily, parameters of applied pressure and speed could regulate dimensions of the shell width as prediction according to pre-experiments before formal printing.

3.2. Metamechanical design

In this section, two types of silicone inks were used, with the tougher one being SE1700 (undyed) and the softer one Ecoflex 30 (dyed red). SE1700 is a type of PDMS, while Ecoflex is platinum-catalyzed silicone, and the PDMS, Ecoflex, or blender are often utilized as a matrix for functional soft materials [52–55]. Hence, we have taken those silicone inks with different mechanical properties than the two building inks for the filament. Using mcDIW, we deposited several filaments for material gradient lattices for tunable stiffness elastic lattice, soft pneumatic fingers. Shown in figure 4, we conducted both simulations and tensile experiments on four types of filaments with different material distribution, i.e. (1) tough, (2) soft, (3) soft core and tough shell, (4) segmented tough and soft, each

measuring 20 mm in length and 1.1 mm in shell width. Both simulated and experimental results revealed that mechanical behavior of filaments could be tailored at millimeter scale through segmented and coaxial multi-material distribution, which could guide further structure design.

As illustrated in figure 5(a), we constructed simple five types of cubic (SC) woodpile structures [56, 57] which was engineered to investigate the impact of the material distributions. The odd layer (along the x -axis) and even layer (along the y -axis) were placed orthogonally to form identical architecture. Notably, for convenient representation, blue lines denote the tough segment (SE 1700), red lines correspond to the soft segment (Ecoflex/SiO₂), the orange lines represent segments with core-shell structures. The lattice samples possess dimensions of $30 \times 30 \times 9 \text{ mm}^3$, where each layer is precisely printed with a height of 0.9 mm, filament width of 1.1 mm and spacing distance of 3 mm. As shown in figure 5(b), the behaviors of samples under tension are mainly determined by filaments along the tensile direction. Specifically for the type 2 sample, the soft filament along the x -axis introduced a lower reactive force than the tough filaments along the y -axis because filament align tension direction undertook most of strain and stress. The compressive behaviors of these lattices in figure 5(c) revealed three typical stages and feature parameters (i.e. ϵ_1 , ϵ_2 , σ_{1s} , E_1 , E_2) [58] in the strain-stress curves. We demonstrated that the capability of mcDIW can adjust those parameters via materials distribution. According to simulation results, the column consisting of intersecting nodes along the

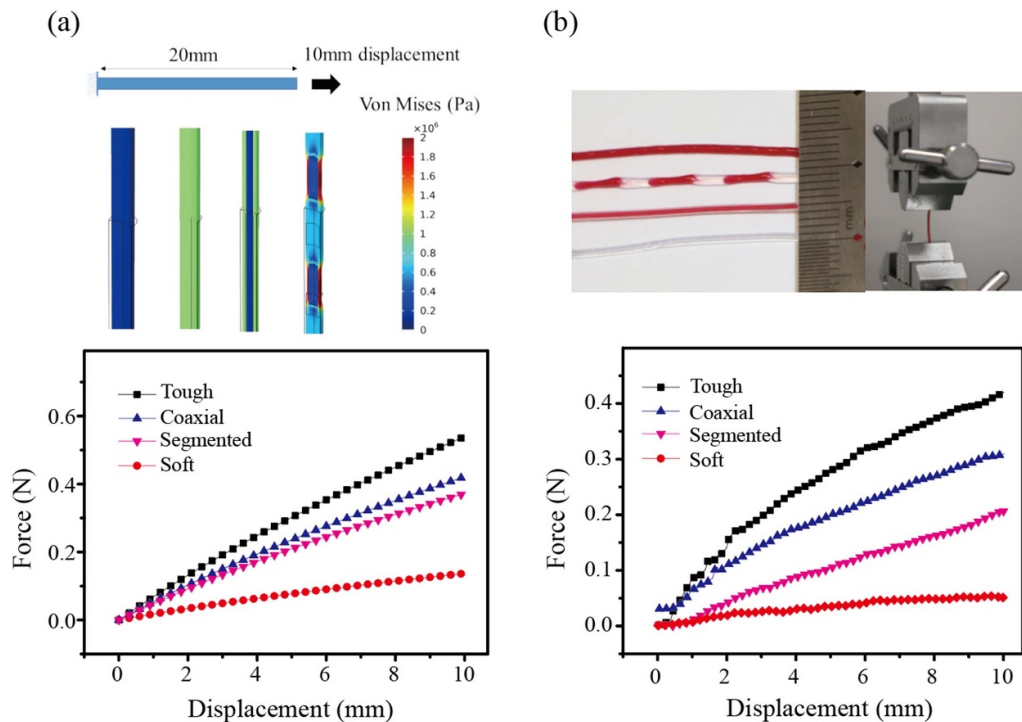


Figure 4. The relationship between displacement and reactive force of four types of filaments including tough, soft, coaxial and segmented filaments. (a) Simulation result; (b) experiment result.

vertical direction (z -direction) attributed to the linear deformation and buckling, corresponding to the linear (up to strain ε_1) and plateau (from ε_1 to ε_2) region of the stress–strain curve shown in figure 5(c).

As for the third stage corresponding to densification stage that strain is beyond ε_2 , all parts of the lattice resist the indenter consistently so the stress–strain curves presented non-linear upward trends. Furthermore, we found similar result along experimental strain–stress curves, presenting tunable stiffness lattice via mcDIW to change compression parameters. Additionally, the type 1 and 5 samples had similar linear and plateau stages but the latter exhibited the lower stress during densification stage since that tougher segments in type 5 sample were placed on internode position, while the softer segments offer less stress in densification stage than that in type 1.

3.3. Soft biomimetic application

In this section, we presented potential of mcDIW in biomimetic field. For instant, four gear-rack like soft fingers are fabricated by our mcDIW with SE1700 and Ecoflex/SiO₂ inks shown in figures 6(a) and (b). Furthermore, their entire teeth were printed in (1) with a tough material and (2) with a soft material, (3) the upper half of teeth printed with a soft material and the lower half a tough material, and (4) the upper half of teeth printed with a tough material and the lower half a soft material. While applying a pressure of 30 kPa (see video S4),

those printed teeth made soft fingers bend with different travel and motion patterns, which is in good agreement with simulation results.

According to figure 6(c), the general fabrication process of the soft magnetic device are classified as five steps: (1) blend silicone matrix and NeFeB particles to form uniform ink, (2) use high impulse magnetic impulse field (5.7 T) to magnetize particles inside ink; (3) print the predefined samples; (4) orientate particles inside the structure by an external magnetic field (e.g. 100 mT); (5) cure specimen in oven at 90 °C for 1.5 h. As shown in figure 6(d), printed magnetic parts composed of coaxial printed filaments while link line was pure silicone using a other parameter to form separation between each line. (SE 1700). It should be noted that in step (5), i.e. orientation, shell ink restricted the magnetic particles from moving too much thus the filament no longer formed straight line (see figure S7).

As shown in figure 6(e), we fabricated a simply soft inchworm-like robot that could crawl via the motion of magnetic parts serving as ‘legs’ under extra magnetic field. The parts at the two ends of the sheet were magnetized as the S pole that is facing outward, while the one in the middle was magnetized reversely. The other parts as ‘body’ linking the ‘legs’, was printed as separated lines for flexibility in all movable directions and further weaving method. As indicated in figure 6(e), about 5 mm march of the robot in an attempt to crawl was achieved under rotation and translation of magnetic filed.

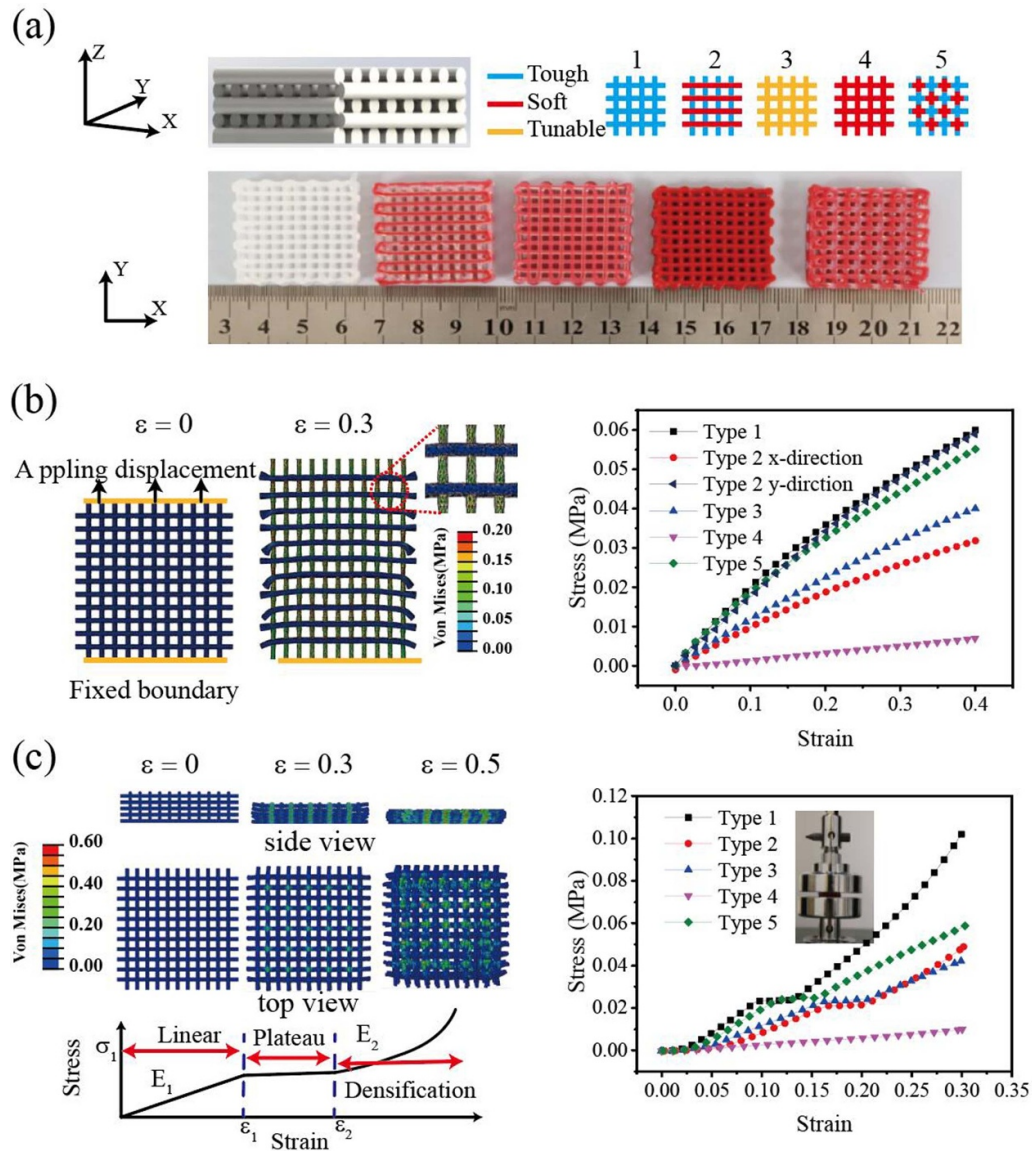


Figure 5. Tunable stiffness printed soft lattices. (a) Illustration of five types of woodpile lattices classified by the alignment of filaments with two layers. Also shown are these printed samples; (b) tensile simulation and experimental stress–strain curves; (c) compression simulation and typical stress–strain for cellular foam, showing the linear, plateau and densification stages. Experimental stress–strain curve measured for the printed samples.

Additionally, as demonstrated in figure 6(f), these sheets with magnetic components, taken as block units, can be intricately woven together to construct soft devices. The top row in figure 6(f) shows the woven structure including magnetic parts where could be set pole orientation independently.

Consequently, the two side columns initiated an inward bending motion when subjected to a magnetic field of 50 mT. As increasing a magnetic field to 200 mT, the structure completely grasped as shown in bottom row of figure 6(f). A detailed visualization of this grasping process can be observed in video S3.

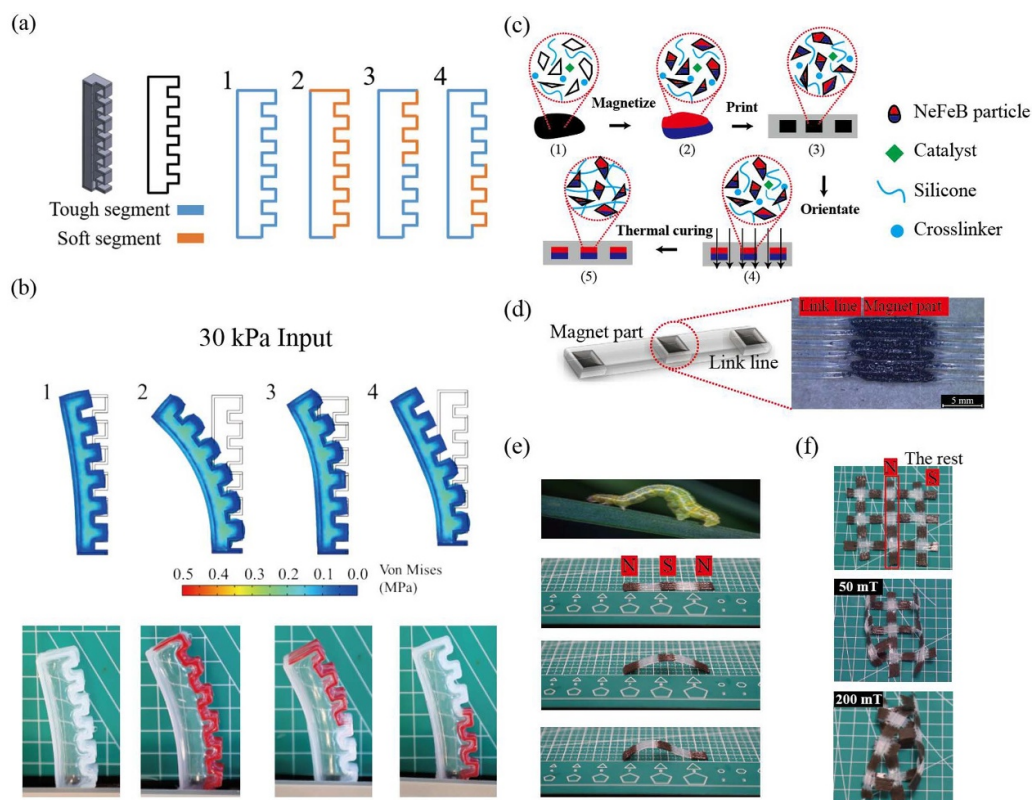


Figure 6. Design and fabrication of gear-rack like and inchworm-like soft robots based on the mcDIW method. (a) Four types of gear-rack like robots having the same dimensions but different adjustable expand segments. (b) The simulation and experiment results under a pneumatic input pressure of 30 kPa. (c) The ink preparation, magnetization, printing, orientation and curing process for fabricating magnetic sample. (d) Linear sheet units for assembly of more complex structures, containing magnetic part and separated linking line. (e) A photograph of a live inchworm (1st row) and crawling of the sheet unit with three magnetic parts, whose specific pole is facing outward and are marked. The sheet unit crawls (3rd to 5th rows) under an applied magnetic field (f) the 2D structure weaved by sheet units, is able to shape shift when applied magnetic field. The pole of each magnetic part is signed in first row graph.

4. Conclusion

In summary, we have presented a multi-material 3D printing approach, i.e. mcDIW, for constructing soft functional devices. Our method can readily control material distributions in millimeter level for 3D-printed filaments, avoiding the frequent switching of printheads and/or inks in conventional methods. More specifically, multi-material filaments can be defined as core/shell or segmented structures with the proposed concurrent and alternating modes. High manufacturing efficiency and accurate registration of the segments are established for meta-mechanical and biomimetic applications. By integrating printheads with other composites, this multimode extrusion method can be utilized for creating complicated soft functional devices.

Data availability statement

The data cannot be made publicly available upon publication because they are not available in a format that is sufficiently accessible or reusable by other researchers. The data that support the findings of this study are available upon reasonable request from the authors.

Acknowledgments

We acknowledge the fundings from National Natural Science Foundation of China (Grant Nos. 51875253 and 52175201), Jiangsu Provincial Key Research and Development Program (BE2022069-2) and the Postgraduate Research and Practice Innovation Program of Jiangsu Province (KYCX20_1830) and China Scholarship Council (202206790068).

Authorship Contribution Statement

Jiawen Xu: responsible for most of the investigations, methodology development, data collection/analysis, writing and editing the manuscript.

Yu Liu: responsible for the funding and resources acquisition, supervising the project, revising the manuscript.

Yanbing Cao: responsible for executing the experimental tests.

Xiaolong Wang, Zhenyu Wang, Heng-Yong Nie: revised the manuscript and provided suggestions.

Conflict of interest

The authors declare no conflict of interest.

ORCID iDs

Jiawen Xu  <https://orcid.org/0000-0001-6825-3846>
 Zhenyu Wang  <https://orcid.org/0000-0002-1324-2346>
 Heng-Yong Nie  <https://orcid.org/0000-0002-8287-5171>
 Xiaolong Wang  <https://orcid.org/0000-0003-4210-840X>
 Yu Liu  <https://orcid.org/0000-0002-7945-7462>

References

- [1] Yuk H, Lu B, Lin S, Qu K, Xu J, Luo J and Zhao X 2020 3D printing of conducting polymers *Nat. Commun.* **11** 1604
- [2] Kim Y, Yuk H, Zhao R, Chester S A and Zhao X 2018 Printing ferromagnetic domains for untethered fast-transforming soft materials *Nature* **558** 274–9
- [3] Kim Y, Parada G A, Liu S and Zhao X 2019 Ferromagnetic soft continuum robots *Sci. Robot.* **4** eaax7329
- [4] Dong C, Leber A, Das Gupta T, Chandran R, Volpi M, Qu Y, Nguyen-Dang T, Bartolomei N, Yan W and Sorin F 2020 High-efficiency super-elastic liquid metal based triboelectric fibers and textiles *Nat. Commun.* **11** 3537
- [5] Wu Y, Dai X, Sun Z, Zhu S, Xiong L, Liang Q, Wong M-C, Huang L-B, Qin Q and Hao J 2022 Highly integrated, scalable manufacturing and stretchable conductive core/shell fibers for strain sensing and self-powered smart textiles *Nano Energy* **98** 107240
- [6] Zhang M et al 2019 Printable smart pattern for multifunctional energy-management E-textile *Matter* **1** 168–79
- [7] Li Y, Zhang Z, Li X, Zhang J, Lou H, Shi X, Cheng X and Peng H 2017 A smart, stretchable resistive heater textile *J. Mater. Chem. C* **5** 41–46
- [8] Li G et al 2021 Self-powered soft robot in the Mariana Trench *Nature* **591** 66–71
- [9] Lee H, Jang Y, Choe J K, Lee S, Song H, Lee J P, Lone N and Kim J 2020 3D-printed programmable tensegrity for soft robotics *Sci. Robot.* **5** eaay9024
- [10] Hubbard J D, Acevedo R, Edwards K M, Alsharhan A T, Wen Z, Landry J, Wang K, Schaffer S and Sochol R D 2021 Fully 3D-printed soft robots with integrated fluidic circuitry *Sci. Adv.* **7** eabe5257
- [11] Wang H, Totaro M and Beccai L 2018 Toward perceptive soft robots: progress and challenges *Adv. Sci.* **5** 1800541
- [12] Wang Y et al 2017 A biorobotic adhesive disc for underwater hitchhiking inspired by the remora suckerfish *Sci. Robot.* **2** eaan8072
- [13] Guan Q, Sun J, Liu Y, Wereley N M and Leng J 2020 Novel bending and helical extensile/contractile pneumatic artificial muscles inspired by elephant trunk *Soft Robot.* **7** 597–614
- [14] Guo Y, Guo J, Liu L, Liu Y and Leng J 2022 Bioinspired multimodal soft robot driven by a single dielectric elastomer actuator and two flexible electroadhesive feet *Extreme Mech. Lett.* **53** 101720
- [15] Guo S Z, Qiu K, Meng F, Park S H and McAlpine M C 2017 3D printed stretchable tactile sensors *Adv. Mater.* **29** 1701218
- [16] Chun S, Son W, Kim H, Lim S K, Pang C and Choi C 2019 Self-powered pressure- and vibration-sensitive tactile sensors for learning technique-based neural finger skin *Nano Lett.* **19** 3305–12
- [17] Wang Y, Wu H, Xu L, Zhang H, Yang Y and Wang Z L 2020 Hierarchically patterned self-powered sensors for multifunctional tactile sensing *Sci. Adv.* **6** eabb9083
- [18] Qian X et al 2018 Printable skin-driven mechanoluminescence devices via nanodoped matrix modification *Adv. Mater.* **30** 1800291
- [19] Ze Q, Kuang X, Wu S, Wong J, Montgomery S M, Zhang R, Kovitz J M, Yang F, Qi H J and Zhao R 2020 Magnetic shape memory polymers with integrated multifunctional shape manipulation *Adv. Mater.* **32** e1906657
- [20] Gladman A S, Matsumoto E A, Nuzzo R G, Mahadevan L and Lewis J A 2016 Biomimetic 4D printing *Nat. Mater.* **15** 413–8
- [21] Chen Q, Cao P F and Advincula R C 2018 Mechanically robust, ultraelastic hierarchical foam with tunable properties via 3D printing *Adv. Funct. Mater.* **28** 1800631
- [22] Chen Q, Zhao J, Ren J, Rong L, Cao P F and Advincula R C 2019 3D printed multifunctional, hyperelastic silicone rubber foam *Adv. Funct. Mater.* **29** 1900469
- [23] Guo D, Kang Z, Wang Y and Li M 2021 Design of multi-material soft pneumatic modules *Smart Mater. Struct.* **30** 095006
- [24] Gao W, Yao J, Zhu K, Zhao P and Chen X 2023 Highly sensitive, wide-range pressure sensor based on negative poisson's ratio for human motion detection *IEEE Sens. J.* **23** 12618–25
- [25] Taylor J M, Perez-Toralla K, Aispuro R and Morin S A 2018 Covalent bonding of thermoplastics to rubbers for printable, reel-to-reel processing in soft robotics and microfluidics *Adv. Mater.* **30** 1705333
- [26] Ning X, Wang X, Zhang Y, Yu X, Choi D, Zheng N, Kim D S, Huang Y, Zhang Y and Rogers J A 2018 Assembly of advanced materials into 3D functional structures by methods inspired by origami and kirigami: a review *Adv. Mater. Interfaces* **5** 13
- [27] Banerjee H, Leber A, Laperrousaz S, La Polla R, Dong C, Mansour S, Wan X and Sorin F 2023 Soft multimaterial magnetic fibers and textiles *Adv. Mater.* **35** e2212202
- [28] Sun J, Liao W and Yang Z 2023 Additive manufacturing of liquid crystal elastomer actuators based on knitting technology *Adv. Mater.* **35** 2302706
- [29] Shi X et al 2021 Large-area display textiles integrated with functional systems *Nature* **591** 240–5
- [30] Ranzani T, Russo S, Bartlett N W, Wehner M and Wood R J 2018 Increasing the dimensionality of soft microstructures through injection-induced self-folding *Adv. Mater.* **30** 1802739
- [31] Tao H and Gibert J 2020 Multifunctional mechanical metamaterials with embedded triboelectric nanogenerators *Adv. Funct. Mater.* **30** 2001720
- [32] Truby R L and Lewis J A 2016 Printing soft matter in three dimensions *Nature* **540** 371–8
- [33] Lind J U et al 2017 Instrumented cardiac microphysiological devices via multimaterial three-dimensional printing *Nat. Mater.* **16** 303–8
- [34] Truby R L, Wehner M, Grosskopf A K, Vogt D M, Uzel S G M, Wood R J and Lewis J A 2018 Soft somatosensitive actuators via embedded 3D printing *Adv. Mater.* **30** 1706383
- [35] Skylar-Scott M A, Mueller J, Visser C W and Lewis J A 2019 Voxelated soft matter via multimaterial multinozzle 3D printing *Nature* **575** 330–5
- [36] Boley J W, van Rees W M, Lissandrello C, Horenstein M N, Truby R L, Kotikian A, Lewis J A and Mahadevan L 2019 Shape-shifting structured lattices via multimaterial 4D printing *Proc. Natl Acad. Sci. USA* **116** 20856–62
- [37] Chen D and Zheng X 2018 Multi-material additive manufacturing of metamaterials with giant, tailorable negative poisson's ratios *Sci. Rep.* **8** 9139
- [38] Zhu Z, Park H S and McAlpine M C 2020 3D printed deformable sensors *Sci. Adv.* **6** eaba5575
- [39] Yang Y, Li X, Zheng X, Chen Z, Zhou Q and Chen Y 2018 3D-printed biomimetic super-hydrophobic structure for

- microdroplet manipulation and oil/water separation *Adv. Mater.* **30** 1704912
- [40] Emon M O F, Alkadi F, Philip D G, Kim D-H, Lee K-C and Choi J-W 2019 Multi-material 3D printing of a soft pressure sensor *Addit. Manuf.* **28** 629–38
- [41] Duoss E B *et al* 2014 Three-dimensional printing of elastomeric, cellular architectures with negative stiffness *Adv. Funct. Mater.* **24** 4905–13
- [42] Mueller J, Lewis J A and Bertoldi K 2021 Architected multimaterial lattices with thermally programmable mechanical response *Adv. Funct. Mater.* **32** 2105128
- [43] Wan X, Luo L, Liu Y and Leng J 2020 Direct ink writing based 4D printing of materials and their applications *Adv. Sci.* **7** 2001000
- [44] Ober T J, Foresti D and Lewis J A 2015 Active mixing of complex fluids at the microscale *Proc. Natl Acad. Sci. USA* **112** 12293–8
- [45] Raney J R, Compton B G, Mueller J, Ober T J, Shea K and Lewis J A 2018 Rotational 3D printing of damage-tolerant composites with programmable mechanics *Proc. Natl Acad. Sci. USA* **115** 1198–203
- [46] Hassan I and Selvaganapathy P R 2022 A microfluidic printhead with integrated hybrid mixing by sequential injection for multimaterial 3D printing *Addit. Manuf.* **50** 102559
- [47] Chen Y, Liu Y, Ren J, Yang W, Shang E, Ma K, Zhang L, Jiang J and Sun X 2020 Conformable core-shell fiber tactile sensor by continuous tubular deposition modeling with water-based sacrificial coaxial writing *Mater. Des.* **190** 108567
- [48] Yu L, Parker S, Xuan H, Zhang Y, Jiang S, Tousi M, Manteghi M, Wang A and Jia X 2020 Flexible multi-material fibers for distributed pressure and temperature sensing *Adv. Funct. Mater.* **30** 1908915
- [49] Cipollone D, Mena J A, Sabolsky K, Sabolsky E M and Sierros K A 2022 Coaxial ceramic direct ink writing on heterogenous and rough surfaces: investigation of core-shell interactions *ACS Appl. Mater. Interfaces* **14** 24897–907
- [50] Chortos A, Mao J, Mueller J, Hajiesmaili E, Lewis J A and Clarke D R 2021 Printing reconfigurable bundles of dielectric elastomer fibers *Adv. Funct. Mater.* **31** 2010643
- [51] Yuk H and Zhao X 2018 A new 3D printing strategy by harnessing deformation, instability, and fracture of viscoelastic inks *Adv. Mater.* **30** 1704028
- [52] Kouediatouka A N, Liu Q, Mawignon F J, Wang W, Wang J, Ruan C, Yeo K F H and Dong G 2023 Sensing characterization of an amorphous PDMS/Ecoflex blend composites with an improved interfacial bonding and rubbing performance *Appl. Surf. Sci.* **635** 157675
- [53] Li M, Chen S, Fan B, Wu B and Guo X 2020 Printed flexible strain sensor array for bendable interactive surface *Adv. Funct. Mater.* **30** 2003214
- [54] Mariello M, Fachechi L, Guido F and De Vittorio M 2021 Multifunctional sub-100 μm thickness flexible piezo/triboelectric hybrid water energy harvester based on biocompatible AlN and soft parylene C-PDMS-Ecoflex™ *Nano Energy* **83** 105811
- [55] Vaicekauskaite J, Mazurek P, Vudayagiri S and Skov A L 2020 Mapping the mechanical and electrical properties of commercial silicone elastomer formulations for stretchable transducers *J. Mater. Chem. C* **8** 1273–9
- [56] Durban M M *et al* 2018 Custom 3D printable silicones with tunable stiffness *Macromol. Rapid Commun.* **39** 1700563
- [57] Maiti A, Small W, Lewicki J P, Weisgraber T H, Duoss E B, Chinn S C, Pearson M A, Spadaccini C M, Maxwell R S and Wilson T S 2016 3D printed cellular solid outperforms traditional stochastic foam in long-term mechanical response *Sci. Rep.* **6** 24871
- [58] Zhu X, Chen Y, Liu Y, Deng Y, Tang C, Gao W, Mei J, Zhao J, Liu T and Yang J 2018 Additive manufacturing of elastomeric foam with cell unit design for broadening compressive stress plateau *Rapid Prototyp. J.* **24** 1579–85